metals

MDPI

Article

Effects of Welding Speed and Pulse Frequency on Surface Depression in Variable Polarity Gas Tungsten Arc Welding of Aluminum Alloy

Jun Du *, Guangxi Zhao and Zhengying Wei

State key Laboratory of Manufacturing System Engineering, Xi'an Jiaotong University, Xi'an 710049, China; zgx6464946@stu.xjtu.edu.cn (G.Z.); zywei@mail.xjtu.edu.cn (Z.W.)

* Correspondence: jundu2010@mail.xjtu.edu.cn

Received: 24 December 2018; Accepted: 21 January 2019; Published: 23 January 2019



Abstract: A three-dimensional (3D) numerical model with the volume of fluid method is developed for high-speed variable polarity gas tungsten arc welding (VP-GTAW) of aluminum alloys. It predicts the thermal flow field in the weld pool, the weld pool surface deformation, and solidified bead geometry during VP-GTAW in successive welding passes. Verification of the numerical model was performed by comparing the calculated results with metallography of welded cross-sections. The prediction showed reasonable accuracy in predicting weld bead geometry. The prediction average relative errors of the bead width and depth of penetration are less than 7%. The deformed weld pool surface, the fluid flow in the weld pool, and maximum fluid temperature in the workpiece based on the developed model, are discussed in detail. The effects of welding speed and pulse frequency on surface depression are studied. The results show that the maximum fluid temperature is closely correlated to the welding speed and pulse frequency. Further, the upper and lower limit of maximum fluid temperature would provide a clue by which the surface depression and the pitch of humps may be recognized. An increase in welding speed will lead to the increase of the pitch of humps, but the reverse is true in the pulse frequency. These detailed physical insights facilitate the prediction of welding surface defects in the high-speed VP-GTAW of aluminum alloy.

Keywords: variable polarity gas tungsten arc welding; surface depression; aluminum alloy

1. Introduction

Aluminum alloys have been widely utilized in engineering structures due to some advantageous properties such as high strength to weight ratio, high conductivity, and ease of machinability [1]. As an essential process of joining metals, welding can create coalescence via heat input. However, welding of aluminum alloys is considered challenging since the welding defects, such as oxide formation, porosity, hot cracking and incomplete fusion, are usually difficult to be accurately characterize and eliminate. Variable polarity-gas tungsten arc welding process has thus far been the most industrially accepted welding process for aluminum and its alloys [2], which can use advanced power supply to precisely control weld heat input and adjust the electrode positive (EP) and electrode negative (EN) independently to enable a good cleaning effect and depth of penetration.

The formation of bead defects and the quality of welds are directly affected by thermal flow behaviors and quantitative analysis of heat transfer, as well as fluid flow in the weld pool being necessary [3–5]. Therefore, the research on the weld pool from the viewpoint of thermal fluid science has always been an important issue in the field of welding [2,6,7]. Earlier studies of weld pool temperature heavily rely on the experimental results and observations. Chen et al. [8] used an infrared camera to monitor the temperature distribution around the weld pool and found that there exists an

exponential relationship between penetration depth and the temperature profile. Vasudevan et al. [9] also measured the temperature profile of weld pool using an IR camera and the computed temperature gradient of weld pool during GTA welding process. In another article, Liang et al. [10] experimentally estimated the cooling curves in the welding of AZ31B magnesium alloy using thermocouples. Although these experimental results can provide an improved understanding of welding process, they cannot reveal the physical mechanism responsible for the surface depression and humping phenomenon. In addition, owing to the presence of plasma in the vicinity of a weld pool, the opacity of liquid metals, and small size of the weld area, the experimental measurement of temperature and velocity fields are extremely difficult to perform. What is more, some detailed information, including the transient thermal-flow behaviors of the liquid metal and the quantitative relationships among the welding process parameters, thermal flow fields in weld pools and final weld bead shape, will be not available from the experimental results and observations.

Over the years, many theories and models have been put forward to study the thermal flow behaviors and weld bead shape in a GTAW process. Dutta et al. [11] turned to numerical methods for the analysis of 3D fluid flow, heat transfer, and mass transport in a moving GTAW process by considering non-axisymmetric boundary conditions, and it was found that the weld pool dynamics is strongly dependent on the relative locations of the clamping device and the electrode. Farzadi et al. [12,13] predicted the local weld pool geometry, weld thermal cycle, and velocity distributions in the weld pool during GTAW of aluminum alloys under steady-state conditions. Wang et al. [2] investigated the weld bead width and solidification characteristics of VP-GTAW welds with different duty ratios of direct current electrode positive (DCEP). Amir et al. [14] calculated the weld pool dimensions in stationary GTAW of pure aluminum using a 2D model. Recently, Pan et al. [7,15] investigated the weld pool dynamics and the formation of weld bead during VP-GTAW of aluminum alloy with filler metal. Meng et al. [16] studied the undercut and humping defects in high-speed GTAW using numerical modelling. Although some achievements had been made by the previous research, there were still some problems existing. All of the abovementioned models showed the complicated phenomena of the GTAW process, but in the existing studies on the VP-GTAW, what kind of relationship exists between the maximum fluid temperature inside workpiece and transient diminution of weld pool was not considered. What is more, a majority of the previous numerical models were related to steel, and aluminum alloy welds produced without filler metal and under non-steady-state conditions received less attention.

The object of this study is to make clear the correlations between the welding process parameters (welding speeds and pulse frequency), weld pool 3D thermal-flow behaviors, and weld bead shape in a moving VP-GTA welding of aluminum alloys. To realize the object, a 3D numerical model of VP-GTA welding was established first. Then, the comparison between the calculated cross-sectional profile of weld bead and the corresponding measured results for the sample was made to verify the established model's accuracy. The transient diminution of weld pool in high-speed VP-GTA welding was systematically analyzed from the viewpoint of maximum fluid temperature history and thermal flow fields in and around the weld pool. Finally, the effects of welding speed and pulse frequency on the surface depression on the surface of a weld bead were investigated.

2. Materials and Methods

2.1. Experimental Procedure

The base material was 2024 aluminum alloy in initial T6 condition with a thickness of 6 mm. The material was cut into several pieces with 300 × 60 × 6 mm^3 dimensions. The nominal chemical composition of the base metal is shown in Table 1. Pure argon (99%) was employed as a shielding gas with flow rates of 15–18 L/min for VP-GTAW.

Table 1. Chemical composition (wt.%) of 2024 aluminum alloy.

Material	Cu	Mg	Mn	Si	Zn	Ti	Al
AA2024	4.52	1.4	0.61	0.16	0.08	0.05	*Bal.*

In VP-GTAW welding system, a Fronius MagicWave 3000 welding power source (Fronius International GmbH, Pettenbach, Austria) was adopted. The VP-GTA welding process used was square wave AC mode. Before welding, oil and other impurities were removed using acetone. The arc welding parameters applied in the experiments are presented in Table 2. Among them, the magnitude of direct current electrode negative (DCEN) welding current is I_{en}, the magnitude of direct current electrode positive (DCEP) welding current is I_{ep}, the welding speed is u, and the pulse frequency is f. The DCEP duty ratio of the VP arc was fixed at 50%.

Table 2. Parameters for VP-GTA welding of aluminum.

Test Case	Adjustable Parameters		Other Fixed Parameters
	f (Hz)	u (mm/s)	
T1	3	5	I_{en}/I_{ep} = 240/120 A U_{en}/U_{ep} = 12.0/11.2 V $\sigma_{j,\,en}/\sigma_{j,\,en}$ = 2.70/2.62 mm $\sigma_{q,\,en}/\sigma_{q,\,ep}$ = 2.70/2.62 mm $\sigma_{p,\,en}/\sigma_{p,\,ep}$ = 3.00/2.92 mm η_{en}/η_{ep} = 0.8/0.5
T2	3	6	
T3	3	7	
T4	1	8	
T5	3	8	
T6	5	8	
T7	10	8	

After the experiments, the samples for metallographic observations were prepared by sectioning the welded joints along the vertical direction using an electrical discharge wire cutting machine (Suzhou Simos CNC Technology Co., Ltd., Suzhou, China). Then, the samples were etched with modified Keller solution (50 mL H_2O, 1 mL HCl, 1.5 mL HF, and 2.5 mL HNO_3) after the processes of rough grinding, fine grinding, and polishing. The microstructure of the treated specimen was observed by Eclipse MA200 light microscope (OM) (Nikon Instruments (Shanghai) Co., Ltd., Shanghai, China).

2.2. Numerical Modelling of VP-GTAW Process

2.2.1. Physical Model Assumptions

A numerical model coupling electromagnetism force, heat transfer, and fluid flow in weld pool is derived in this section. The electric arc is modeled using an equivalent heat source applied to the upper surface of a workpiece. A Gaussian distribution function can be used to describe the modeled electric arc quantities. It was assumed that the welding torch moves at a constant welding speed. The electromagnetic, continuity, momentum, and energy equations can be solved in the weld pool. The considered problem possesses symmetry with respect to the longitudinal vertical median plane and can therefore be calculated as half a plate.

The understanding of VP-GTA welding process by numerical modelling needs the knowledge of the influence of various process variables, including type of shielding gas and shielding gas flow rate. It is well known that the shielding gas parameters can obviously change the thermal properties of solidified weld. A lower shielding gas flow rate can result in an increase in temperature [17], which will promote the heat flux being diffused within a shorter space of time. Other studies, including Ley [18], have explored reducing the shielding gas flow rate to improve the thermal conductivity of the weld. A lower shielding gas flow rate showed several beneficial properties such as low thermal expansion, high specific heat capacity, and thermal conductivity. However, too high a flow rate can cause poor penetration and/or porosity. Up to now, there is no direct literature addressing the quantitative relation of shielding gas flow rate and weld bead dimensions during the VP-GTAW process. There is

an optimum flow rate for weld shielding gases, but this is often decided by preference or experience. In this study, the weld region is protected from atmosphere by pure argon (Ar) gas, and the flowing rate of the shielding gas was 15–18 L/min.

2.2.2. Governing Equations

The numerical simulation of heat and mass transfer processes are governed by a set of equations in a Flow-3D (V11.1.5, Flow Science, Santa Fe, NM, USA) model. In the present study, the liquid metal is assumed to be incompressible Newtonian fluid, and the flow should be laminar. Thus, the governing equations can be simplified as follows:

Mass conservation equation:

$$\nabla \cdot \vec{V} = 0 \tag{1}$$

where $\vec{V}$ denotes the velocity vector.

Momentum equation:

$$\frac{\partial \vec{V}}{\partial t} + \vec{V} \cdot \nabla \vec{V} = -\frac{1}{\rho} \nabla P + \frac{\mu}{\rho} \nabla^2 \vec{V} - \mathrm{K}\vec{V} + G \tag{2}$$

where t is the time, P is the pressure, ρ is the fluid density, K is the drag coefficient, η is the dynamic viscosity, and G is the acceleration by body force.

Energy equation:

$$\frac{\partial h}{\partial t} + \vec{V} \cdot \nabla h = \frac{1}{\rho} \nabla \cdot (k \nabla T) \tag{3}$$

$$h = \begin{cases} \rho_s \rho_s T & (T \le T_s) \\ h(T_s) + h_{sl} \dfrac{T - T_s}{T_l - T_s} & (T_s \le T \le T_l) \\ h(T_l) + \rho_l C_l (T - T_l) & (T_l \le T) \end{cases} \tag{4}$$

where h is the enthalpy, T is the local temperature, k is the thermal conductivity, ρ_s is the solid density, ρ_l is the fluid density, C_l and C_s are specific heat of liquid and solid phases, h_{sl} is the latent heat of fusion, and T_l and T_s are liquidus and solidus temperatures. For the binary aluminum alloys, liquidus temperature/composition relations can easily be derived from highly accurate binary diagrams. These are based on experimental data obtained under equilibrium solidification conditions. T_s is temperature of the end of crystallization, the point where the ends of multicomponent eutectic crystallization occur and where the alloy is fully crystallized. From this point, transformations in the solid state can only take place due to the decreasing solubility in aluminum with decreasing temperature. The samples from as-deposited materials were taken for the differential scanning calorimetry (DSC) analysis. The DSC was done in a calorimeter using 5 mm diameter discs, which were 3 mm thick and heated at 20 °C/min. This allowed for the determination of the solidus temperatures of the tested alloys.

The free surface tracking of the weld pool surface in VP-GTA welding is solved using the volume of fluid (VOF) method [19].

VOF equation:

$$\frac{\partial F}{\partial t} + \nabla \cdot \left(\vec{V} F \right) = 0 \tag{5}$$

where F is the volume of the fluid.

The interfacial force would be considered using the continuum surface force (CSF) proposed by Brackbill et al. [20]. The tangential stresses in the free surface are considered and the contact angles are applied as an essential boundary condition. The liquid metal density, surface tension, viscosity, and workpiece thermal properties are assumed to change with temp

2.2.3. Boundary Conditions

The electric arc was assumed as an internal boundary condition and can be described as Equation (6):

$$k\frac{\partial T}{\partial \vec{n}} = \dot{q}_{arc} - \dot{q}_{conv} - \dot{q}_{rad} \tag{6}$$

where $\dot{q}_{arc}$, $\dot{q}_{conv}$, and $\dot{q}_{rad}$ are the arc heat input, and convective and radiative heat loss, respectively, and $\vec{n}$ is the surface normal.

In this study, according to the actual processing conditions that the welding current in case of DCEP and DCEN (I_{en}/I_{ep} = 240/120 A) is high enough, arc stiffness and impact force exerted onto the weld pool surface is larger, and the arc column is perpendicular to the surface of the weldment. Therefore, the Goldak's double-ellipsoidal heat source model was adopted [21], which can provide relatively accurate results, especially for the low penetration surface melting process. In the moving volumetric heat source model, the power density distributions of the front and rear quadrants can be described using Equations (7) and (8), respectively:

$$q_r = \frac{6\sqrt{3}q_{arc}f_r}{\pi a_r bc\sqrt{\pi}}\exp\left(-3\left[\frac{x^2}{a_r^2}+\frac{y^2}{b^2}+\frac{z^2}{c^2}\right]\right) \tag{7}$$

$$q_f = \frac{6\sqrt{3}q_{arc}f_f}{\pi a_f bc\sqrt{\pi}}\exp\left(-3\left[\frac{x^2}{a_f^2}+\frac{y^2}{b^2}+\frac{z^2}{c^2}\right]\right) \tag{8}$$

where f_f and f_r are the front and rear fraction of the heat flux; a_f, a_r, b, and c are the parametric values obtained from the metallographic data and the weld bead profile; and q_{arc} is the welding arc heat input.

The heat loss $\dot{q}_{\mathrm{conv}}$ and $\dot{q}_{\mathrm{rad}}$ can be calculated as follows:

$$\dot{q}_{\mathrm{conv}} = h_{\mathrm{conv}}(T - T_0) \tag{9}$$

$$\dot{q}_{\mathrm{rad}} = \varepsilon\sigma_{sb}\left(T^4 - T_0^4\right) \tag{10}$$

According to the Vinokurov's empirical model [22], combined convection-radiation heat transfer coefficient is given as:

$$h_{vino} = 2.41 \times 10^{-3}\varepsilon T^{1.61} \tag{11}$$

The pressure boundary conditions on the weld pool surface can be described using Equation (11):

$$P = P_{arc} + \frac{\gamma}{R_c} \tag{12}$$

where P_{arc} is the arc pressure, and R_c is the curvature radius of the weld pool surface. The surface tension γ can be calculated as follows:

$$\gamma = \gamma_0 - \gamma_T(T - T_l) \tag{13}$$

The arc pressure distribution was assumed to follow the distribution of current density. It can be modeled using a Gaussian model with the same radius of arc drag force, as given below [23]:

$$P_{arc}(x,y) = \frac{\mu_0 I^2}{4\pi^2\sigma_r^2}exp\left(-\left(\frac{r^2}{2\sigma_r^2}\right)\right) \tag{14}$$

where μ_0 is the magnetic permeability of free space, and σ_r is the arc pressure parameter (DCEN phase: $\sigma_r = \sigma_{p,\,en}$; DCEP phase: $\sigma_r = \sigma_{p,\,ep}$)

The arc drag force on the weld pool is greatly dependent on the current, the composition of shielding gas, and the tip angle of electrode. Here, the effect of arc drag force is considered as a spatial boundary distribution, which can be represented as follows [24]:

$$P_{Drag}(r) = P_{Max}\sqrt{\frac{r}{r_{Shear}}}exp - \left(\frac{r}{r_{Shear}}\right)^2 \quad (15)$$

where r_{Shear} is the distribution parameter of arc drag force.

2.2.4. Body Force

The body force mainly includes electromagnetic force (EMF), gravity, and buoyancy. The gravity acceleration is 9.81 m/s^2. The temperature-dependent properties were used for the density. The electromagnetic force, as an important body force, was considered by adopting the elliptically symmetric welding current density [25,26]. The equations relating to the EMF are listed as below.

$$F_x = -J_z \times B_\theta \frac{x}{r_a} \quad (16)$$

$$F_z = -J_r \times B_\theta \quad (17)$$

$$J_z = \frac{I}{2\pi}\int_0^\infty \lambda J_0(\lambda r_a) exp\left(-\frac{\lambda^2\sigma_x}{2}\right)\frac{sinh[\lambda(c-z)]}{sinh(\lambda c)}d\lambda \quad (18)$$

$$J_r = \frac{I}{2\pi}\int_0^\infty \lambda J_1(\lambda r_a) exp\left(-\frac{\lambda^2\sigma_x}{2}\right)\frac{sinh[\lambda(c-z)]}{sinh(\lambda c)}d\lambda \quad (19)$$

$$B_\theta = \frac{\mu_m I}{2\pi}\int_0^\infty J_1(\lambda r_a) exp\left(-\frac{\lambda^2\sigma_x}{2}\right)\frac{sinh[\lambda(c-z)]}{sinh(\lambda c)}d\lambda \quad (20)$$

$$r_a = \sqrt{(x-x_0)^2 + \left[\frac{\sigma_x}{\sigma_y}(y-y_0)\right]^2} \quad (21)$$

where I is the arc current (DCEN phase: $I = I_{en}$, $\sigma_j = \sigma_{j,\,en;}$ DCEP phase: $I = I_{ep}$, $\sigma_j = \sigma_{j,\,ep}$); F_i are the components of the EMF force in the i-direction ($i = x, y, z$); J_z and J_r are the axial and radial current density in the cylindrical coordinate system; B_θ is the angular component of magnetic field; J_0 and J_1 are the zero order and one order Bessel functions, respectively; z indicates the vertical depth from the top surface of workpiece; and c is the workpiece thickness.

2.2.5. Numerical Model

In VP-GTAW for an aluminum alloy, the typical waveform of alternating current is a square wave as shown in the Figure 1. The initial state of the workpiece was taken from the VP-GTAW model, as shown in Figure 2, for which the 3D x-y-z coordinate system was defined on the metal workpiece. A 2D r-z-axis coordinate system was located at the center of the electric arc that moved at a constant speed. The electrode was assumed to travel in the positive direction of x-axis from (x = 8 mm) to (x = 24 mm).

The calculation domain consisted of three parts: the aluminum alloy workpiece in the middle, the air above, and the air below. The continuative boundary conditions were employed for the all external boundaries of computational domain, meaning that the "gas phase" near the boundaries would infinitely extend outside the computational domain. The length of the workpiece was $x \times y \times z$ = 32 mm × 15 mm × 6 mm. A grid size (200 μm) and computational time-step (2.5 × 10^{-6} s) for simulations were used. It took approximate 72 h to run 6 s of real-time simulation of welding using a high-performance computer of 48 × 1.6 GHz CPUs.

Thermo-physical properties of material used in this study are listed in Table 3. The contact angle, defined as the angle at which the liquid metal meets the workpiece surface, was assumed to be 90°.

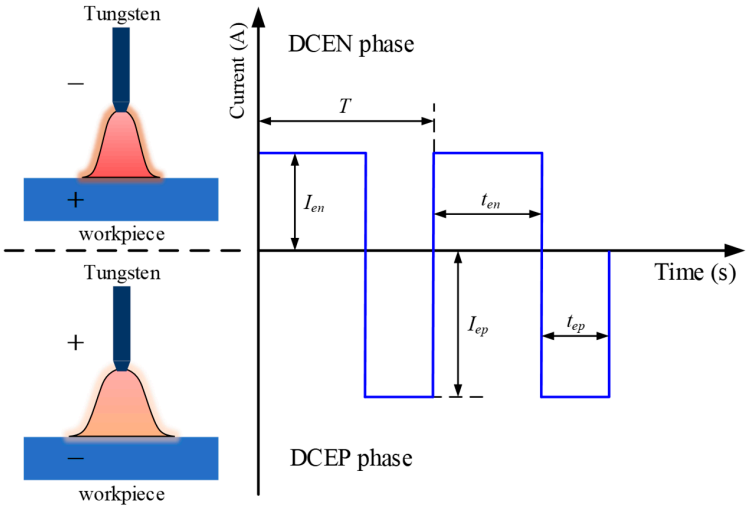


Figure 1. Current waveform of VP-GTAW process.

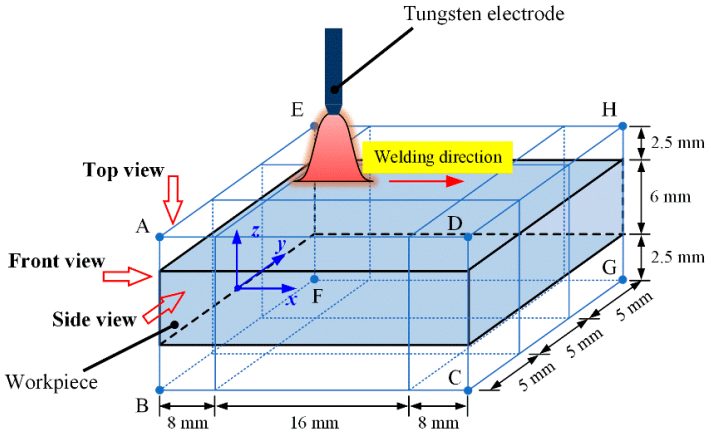


Figure 2. Initial state of the VP-GTAW model.

Many problems of welding encountered in practice involve complicated geometries with complex boundary conditions or variable properties. In fact, some variable thermophysical properties including melt viscosity, density, specific heat, and others have been considered in the present model. These temperature-dependent material properties are plotted in Figure 3. The thermophysical property data calculated using JMatPro Version 9.0 (Sente Software Ltd., London, UK) has been used as direct inputs to simulation software Flow-3D (v11.1.5).

Using improper parameters can lead to excess spatter, creating a need for additional cleanup of welds. Amperage, voltage, and welding feed speed can affect the finished weld if the welding parameters are not properly set. Before starting any modelling project, preliminary experiments were performed to estimate the limits of process maps. The welding parameters (current, voltage, welding speed, etc.) were defined within the range of the machinery (Fronius MagicWave 3000, Fronius International GmbH, Pettenbach, Austria) limits. The constraints of the model were specified due to the validity of the gouging penetration model simplifications. In experiments, the current values can be varied from 95 to 280 A, where the welding speed values varied from 2 to 11 mm/s, depending on the material type.

Parameter determination of the double-ellipsoidal heat source model was obtained from the metallographic data and the weld bead profile. Actually, the heat source parameter estimation and the experimental verification for heat source parameter estimation after welding has been carried out according to References [27,28]. These parameters used for simulation are shown in Table 4. For different processing conditions, the detailed values need to be remeasured.

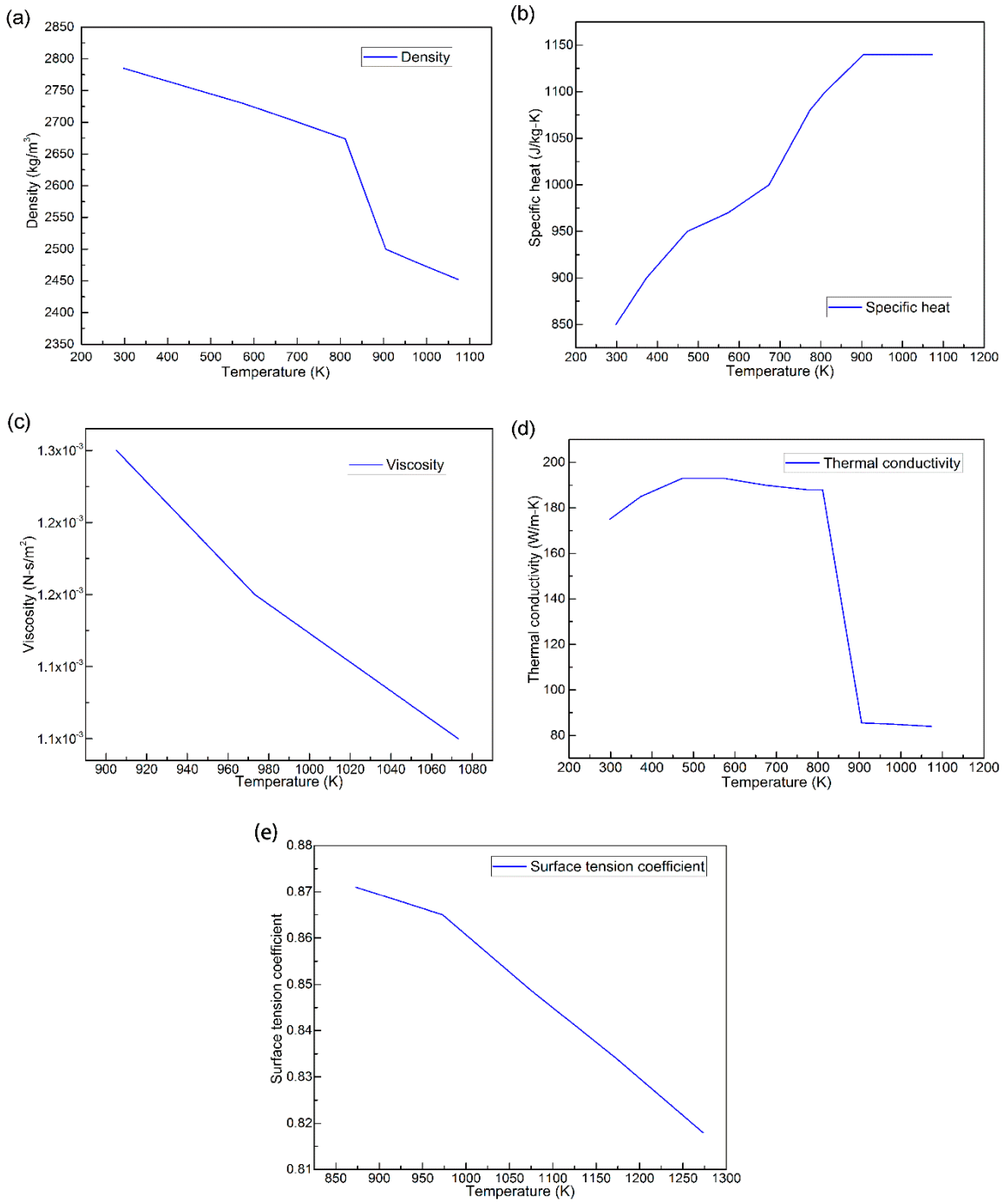


Figure 3. Temperature-dependent thermo-physical properties of 2024 aluminum alloy: (**a**) density, (**b**) specific heat, (**c**) viscosity, (**d**) thermal conductivity, and (**e**) surface tension coefficient.

Table 3. Thermo-physical properties of 2024 aluminum alloy and other process variables.

Properties	Value (Unit)
Density	$f(T)$, Figure 3 (kg m^{-3})
Viscosity	$f(T)$, Figure 3 (N s/m^2)
Surface tension at liquidus temperature	$f(T)$, Figure 3 (N m^{-1})
Thermal conductivity of metal	$f(T)$, Figure 3 (W m^{-1} K^{-1})
Specific heat capacity	$f(T)$, Figure 3 (J kg^{-1} K^{-1})
Solidus temperature	T_s = 811.15 (K)
Liquidus temperature	T_l = 905.15 (K)
Thermal expansion coefficient	$\rho_T = 7.2 \times 10^{-5}$ (1/K)
Emissivity	$\varepsilon = 0.4$
Magnetic permeability	$\mu_0 = 1.26 \times 10^{-6}$ (H m^{-1})
Electrical conductivity	$\sigma_e = 2.5 \times 10^7$ (Ω^{-1} m^{-1})
Ambient temperature	298 (K)
Latent heat of melting	$L = 3.97 \times 10^5$ (J kg^{-1})
Latent heat of vaporization	$L_{ev} = 1.08 \times 10^7$ (J kg^{-1})
Convective heat transfer coefficient	h_c = 100 (W m^{-2} K^{-1})
Vaporization temperature	T_{ev} = 1163 (K)
Ambient temperature	T_∞ = 298 (K)
Moving speeds of the torch	u = 5–8 (mm s^{-1})
Arc thermal efficiency	$\eta_{en} = 0.8$
	$\eta_{ep} = 0.5$

Table 4. Heat source parameters: I_{en}/I_{ep} = 240/120 A, f = 5 Hz, and u = 6 mm/s.

Parameters	Value
Length of front ellipsoidal (mm)	$a_f = 2.7$
Length of rear ellipsoidal (mm)	$a_r = 6.3$
Width of heat source (mm)	$2b = 5.4$
Depth of heat source (mm)	$c = 1.35$
Fraction of heat in front ellipsoidal	$f_f = 0.6$
Fraction of heat in rear ellipsoidal	$f_r = 1.4$

3. Results and Discussion

3.1. Experimental Verification of the Numerical Model

To confirm the predictive accuracy of the established model, the corresponding welding experiments were carried out. The VP-GTA welding process was performed without additional filling material. A cathode with 60° cone angle and a 3.2 mm radius float tip provided a good combination. The distance between the tungsten electrode tip and workpiece surface was fixed at 4 mm. To avoid heat sinks, the workpieces need to be thermally insulated from the fixtures in VP-GTA welding process. In fact, verification and validation of the numerical model were conducted according to one of seven sets of processing parameters in Table 2. The accuracy of the model was evaluated from three respects: characteristic dimension of the humped VP-GTA weld bead, fusion zone size, and the surface temperature of weld pool.

Figure 4a shows the macroscaled top view of the weld bead geometry under the test case T3 in Table 2. It is seen that as one of the most commonly occurring geometric defects, the humping phenomenon has been observed in Figure 4b at higher welding speeds. Unlike the middle portion of a long weld, weld profiles are irregular and unstable because the arc energy, mass, and momentum transfer changes abruptly, thus producing very unsteady temperature and flow fields.

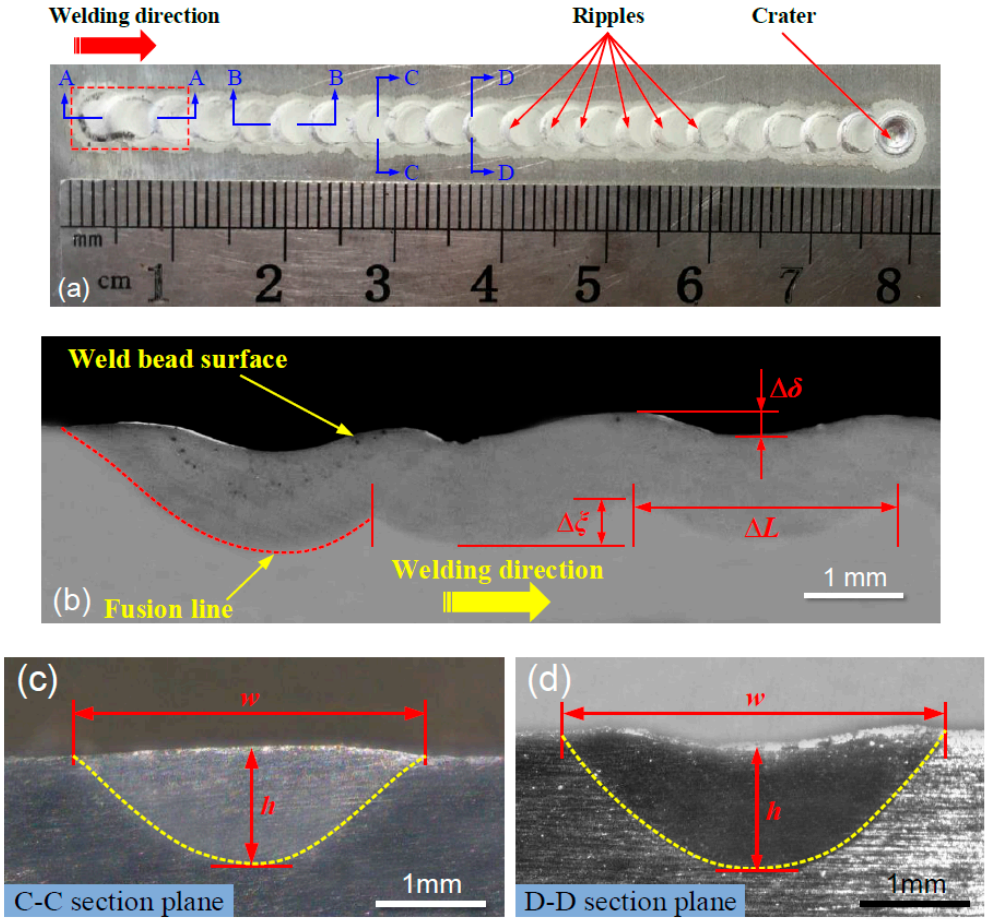


Figure 4. Experimental weld bead shapes for GTA welds achieved under the following conditions: I_{en}/I_{ep} = 240/120 A, f = 3 Hz, and u = 7 mm/s, showing the (**a**) top view of weld bead, (**b**) longitudinal view of the weld, (**c**) transverse cross-section of the weld at the hump, and (**d**) transverse cross-section at a concave weld bead profile.

Figure 4b shows the longitudinal sections of the VP-GTA weld from the beginning portion to the middle portion with regularly spaced humps and valleys. The welding direction was from left to right. Figure 4c,d shows transverse sections at a valley and a hump, respectively, of the humped VP-GTA weld bead in Figure 4a. The cross-sectional shapes of the welded joints are different at the specific locations. The fusion lines are marked in yellow dotted lines on the metallographic images. The weld bead geometry can be characterized by the surface depression of deformed weld pool (longitudinal section: $\Delta\delta$; transverse section: $w/2$) and pitch of the humps (ΔL).

Verifications of the numerical model were carried out by comparing the calculated results with the metallographic macrosections and the surface temperature of the weld pool recorded using infrared thermograph, as shown in Figure 5. Calculated solidus isotherm 811 K (yellow dotted line) corresponds to the fusion line obtained in the experiments. It was found that the calculated weld pool geometries and dimensions agree well with the experimental data. The average values of weld metal width and penetration depth were measured to be 4.65 mm and 1.46 mm, respectively, which is consistent with the calculated results. The calculated average pitches for the case are nearly the same (2.42 mm) as that of the experimental data (2.3 mm). The average relative errors of the weld metal width and penetration depth were less than 7%. The fidelity of the models will be verified to better predict the surface depression for high-speed VP-GTA welding and eliminate the welding defects based on the understanding of its mechanism. The surface temperature of weld pool was recorded using InfraTec VarioCAM hr (FLIR Systems Co., Ltd., Boston, MA, USA), FLIR Systems (FLIR Systems Co., Ltd.,

Boston, MA, USA). The camera with a 384 × 288 pixel resolution was located at a distance of 0.5 m from the workpiece surface, its sensitivity was 0.08 k at 30 °C, minimum focus distance is 0.3 m, the field of view was 24 × 18, the spatial resolution was 0.65 mrad, the electronic 1–8× zoom can shift continuously, and recording frequency reached 50 Hz.

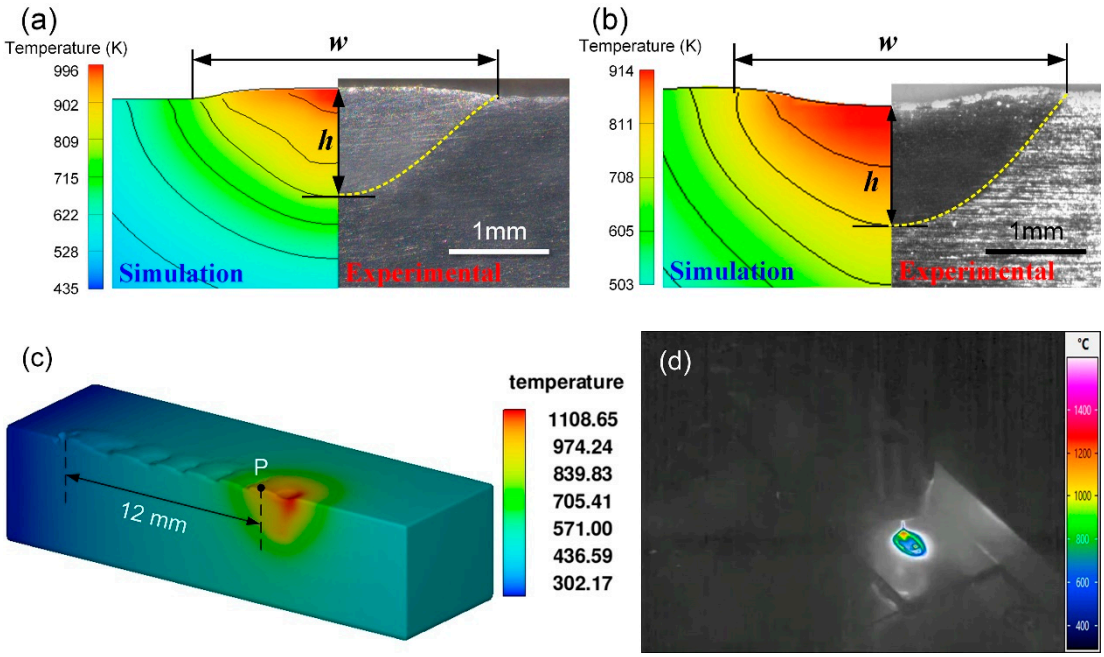


Figure 5. Comparison between the computed thermal profiles (**a**) and experimentally determined (**b**) cross-sections of the C–C and D–D section planes in Figure 4a. (**c**) Calculated weld bead profile and temperature distribution, and (**d**) measured surface temperature distribution of the weld pool using an infrared camera.

Figure 6c,d present the simulated and measured surface temperature of the weld bead recorded using the infrared thermograph. At the specified points P1, the peak temperatures of the simulated and measured are 1011.1 K and 1089.7 K, respectively. The relative error of the peak temperatures at the weld pool surface was about 7.2%, and the agreement between the measured and calculated temperature field distribution is excellent. Moreover, the elapsed time above 905 K, the heating and the cooling rate of the simulated and measured samples were basically consistent with each other, indicating that our simulation has great reliability.

To confirm the insensitivity of the results to resolution, we conducted a time-step independence analysis. A test about the time-step sensitivity for this unsteady simulation, shown in Figure 6, has been performed. Two different time discretizations were used: 2.5×10^{-6} s and 1×10^{-6} s, both of which can present the temperature history at a specified position (8, 0, 0.5 in Figure 5c) well. The temperature variation at the same point was investigated. Figure 6 shows the temperature variation curves calculated based on these two time resolutions. The maximum discrepancy during a welding cycle was 2.41%, which indicates that the bigger time step (2.5×10^{-6} s) was adequate for the unsteady simulation. Therefore, the bulk of the results that we present below will be based on a grid size of 200 µm and a time step of 2.5×10^{-6} s.

Figure 7 shows the side-views ($y = 0$) of thermal-flow fields in the weld pool and its isothermal surfaces during the initial stage of welding. The case was considered at the DCEN/DCEP currents of 240/120 A, the welding speed was 7 mm/s and the pulse frequency was 3 Hz.

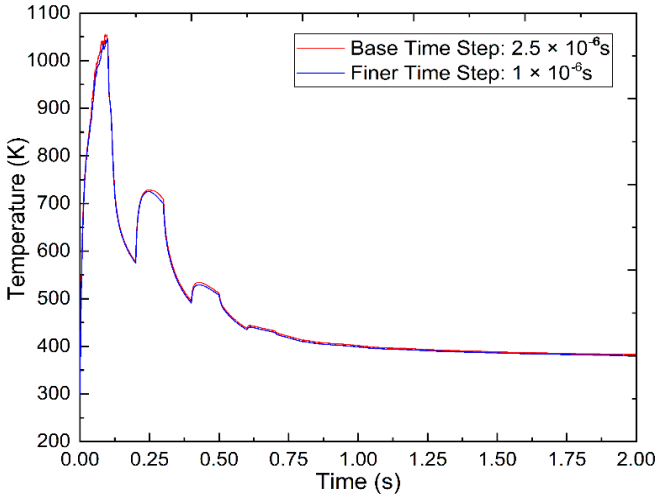


Figure 6. Temperature variation at a specified position for time step sensitivity study.

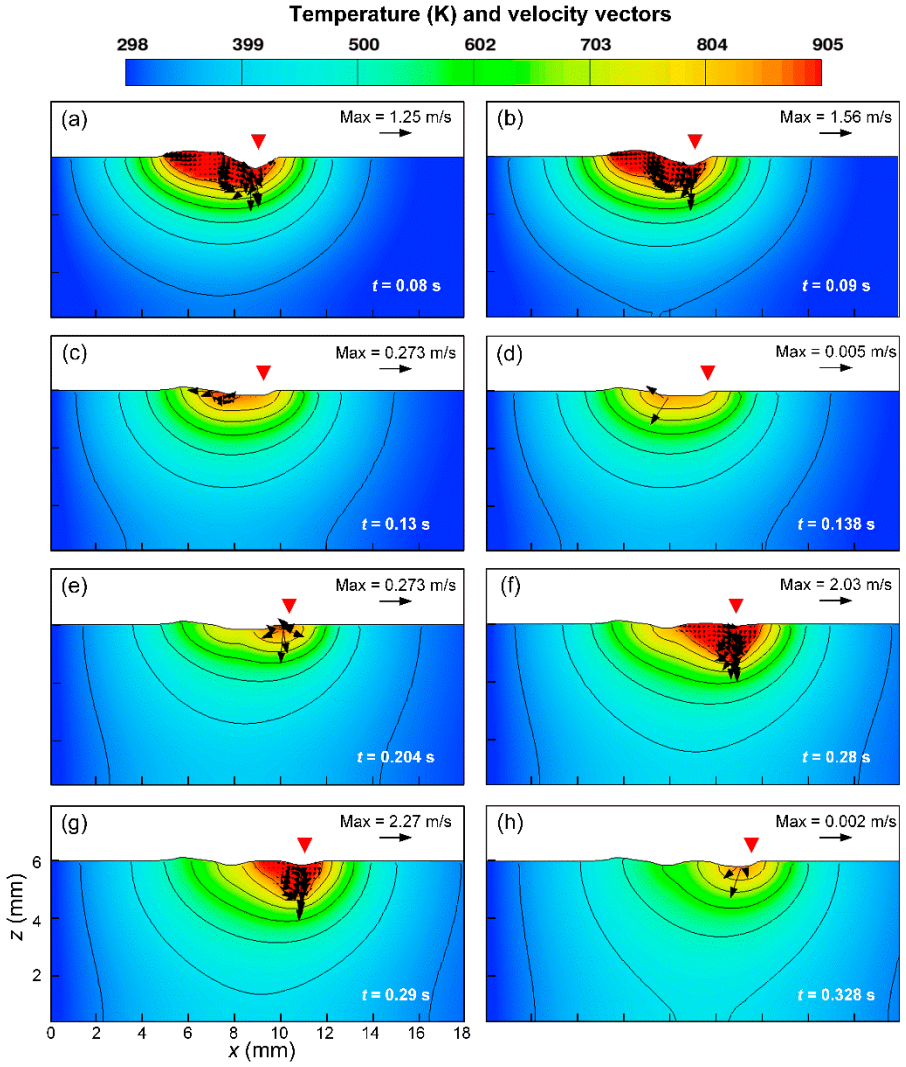


Figure 7. Longitudinal views of temperature and velocity distributions at (**a**) t = 0.08 s, (**b**) 0.09 s, (**c**) 0.13 s, (**d**) 0.138 s, (**e**) 0.204 s, (**f**) 0.28 s, (**g**) 0.29 s, and (**h**) 0.328 s.

As can be seen in Figure 7a, the temperature near the arc center (denoted by the red inverted triangle) was higher and decreased toward the tail of the weld pool. At the beginning stage (t = 0

to 0.08 s), the arc pressure created an obvious surface depression (known as the gouging region) of a VP-GTA weld pool and pushed the high-temperature liquid metal backwards up to a level higher than the workpiece surface. Consequently, a high weld bead was produced at the beginning of welding, then the height gradually decreased as the welding process continued, but the morphology of the solidified bead was generally different from that of the periodic humps.

From t = 0.08 to 0.2 s, as the current turned to its DCEP phase, the arc pressure and Lorentz force decreased, thus the high-level liquid metal tended to fill up the gouging region and the liquid fraction decreased. Meanwhile, the solidification and cooling rate of the molten metal increased significantly as the heat input decreased. The solidifying metal impeded the backfilling of liquid metal and made the liquid channel susceptible to the premature solidification. At t = 0.14 s, the remainder of liquid metal at the tail of the weld pool became completely solidified, so a hump on the weld surface occurs. The arc kept moving from t = 0.14 to 0.2 s, but the heat input in the DCEP phase did not provide enough thermal energy for melting the base metal. As the current turned back to its DCEN phase at t = 0.2 s (Figure 7e), the base metal began to be heated up once again, the temperature and velocity in the weld pool increased, and the liquid level below the arc increased again. At the turning moment of the current, the maximum velocity in the weld pool experienced a sudden rise (Figure 7b); the reasons behind this phenomenon could be attributed to the temporal fluctuations of the local moment and imbalance between upward and downward flow along the walls of the gouging region.

As discussed above, the hump formation was mainly attributed to a combined action of the fluctuation of the dynamic weld pool by an alternating transport current, and the periodical variation of the cooling rates and solidification growth rates in DCEN and DECP phase. At the starting and ending locations, the existence of unsteady and quick liquid motion is observed in the weld pool, and some humps were formed in these locations. Using the pulsed arc source, the up and down fluctuations of the GTA weld pool were clearly observed, which exhibited relatively constant periods, leading to molten metal above the workpiece surface and solid and periodic humps were formed.

To illustrate more clearly, the intermediate stages of the VP-GTA welding were selected to investigate the weld pool evolution. The arc heat source moved to x = 18 mm at about 1 s after the welding experiment started. The regular humps above the surface of the base metal could be obviously seen in Figures 8 and 9, and it is noted that for VP-GTAW of Al alloys, the weld pool solidified quickly due to the its high heat conductivity of Al alloys, which led to a smaller and nearly semicircular weld pool in the xy-plane (Figures 8b and 9b).

Note that at t = 1.35 s, the workpiece was subject to the DCEN current. As can be seen in Figure 8, the weld pool became larger and the penetration was deeper at a higher level of current (I_{en}) due to the intense arc heat. It is observed from Figure 8c that the convection in liquid metal significantly influenced the weld pool shapes. A typical flow pattern of two-vortex (Figure 8a) always coexisted in the weld pool due to the Lorentz force, arc drag force, and negative surface tension temperature gradient.

When the weld pool kept moving from t = 1.35 to 1.5 s, the length of hump valley increased. The workpiece was subjected to the DCEP current, as shown in Figure 9, and the heat input for this situation was lower due to the lower current, thus the fluctuations of surface temperature and high solidification rate occurred. The solidification front velocity increased dramatically with time. At t = 1.5 s, the model predicted a smaller penetration and width, and the lower flow velocity were observed.

The comparison of the weld pool shapes, and the temperature and velocity fields at different times (Figures 8 and 9) demonstrates that the peak temperature at the weld pool surface in the DCEN phase was higher than that at DCEP phase. The temperature above 560 K mainly concentrated within 4 mm from the workpiece surface, as can be seen in Figures 8b and 9b. In Figure 8a, it should also be noted that the weld pool was not symmetrical about the center of the electrode, i.e., the front of the isotherm T = 966 K was approximately 2 mm ahead of the electrode, but the tail was about 3.2 mm behind. The reason for this phenomenon is mainly attributed to the travel of the arc heat

source. Little penetration of the heat input into the welded workpieces was observed in Figure 8c. The difference in temperature between the top and bottom surfaces of the workpiece decreased with a decrease in T. The fluid metal moved from the arc center toward the periphery of the weld pool surface, which indicates that the Marangoni force and arc drag force played an important role in determining the flow patterns in the weld pool. This was because of the combined action of the arc drag force and the temperature gradients on the weld pool surface that enabled surface tension driven flow from a region with low surface tension to another region with high surface tension. Just for these reasons, there is a recirculation zone where the fluid metal flowed from the arc center toward the periphery of the weld pool. Furthermore, it is seemed that the maximum velocity always occurred along the penetration depth.

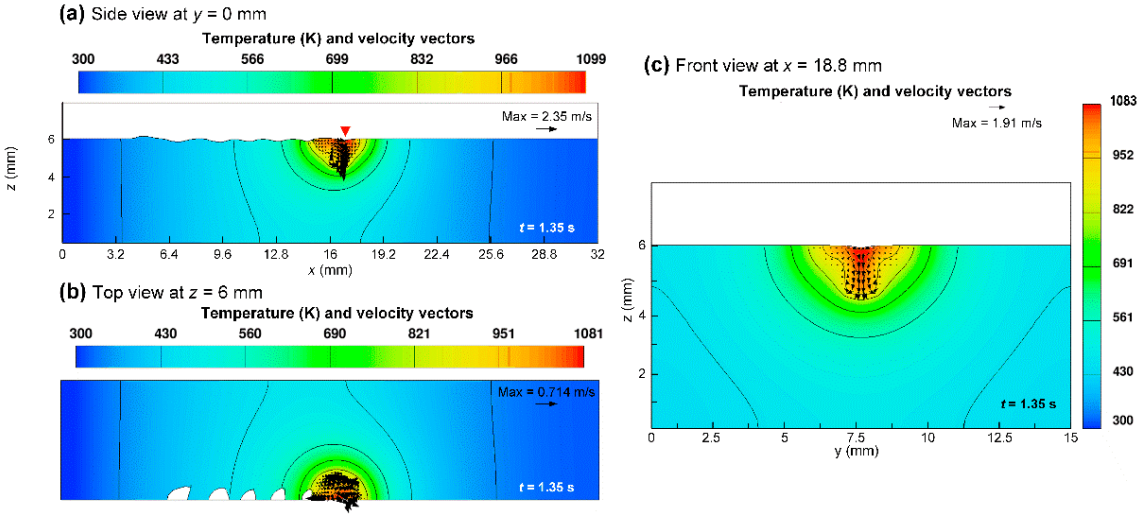


Figure 8. Side views of temperature and velocity distributions under the conditions: I_{en}/I_{ep} = 240/120 A, f = 3 Hz, and u = 7 mm/s showing the (**a**) side view, (**b**) top view, and (**c**) front view.

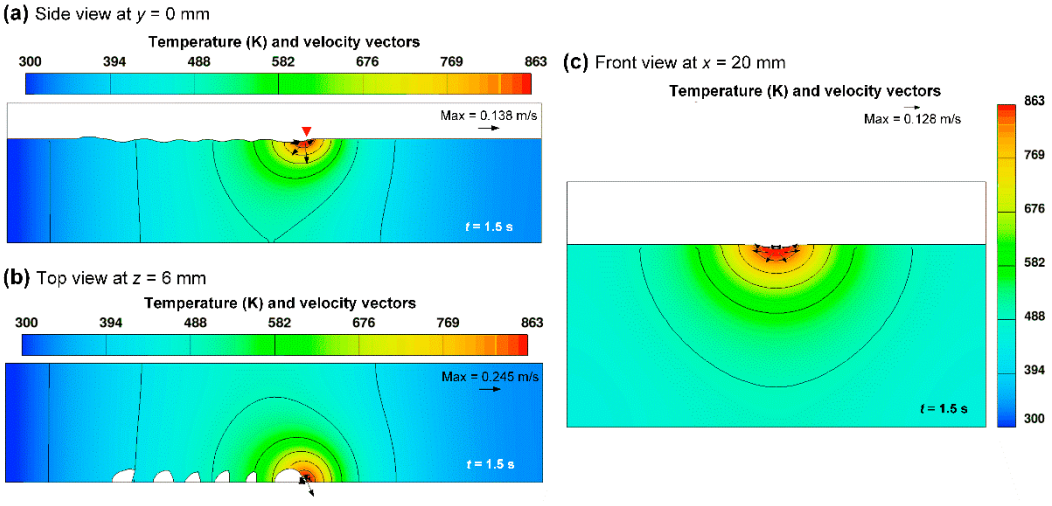


Figure 9. Side views of temperature and velocity distributions under the conditions: I_{en}/I_{ep} = 240/120 A, f = 3 Hz, and u = 7 mm/s showing the (**a**) side view, (**b**) top view, and (**c**) front view.

3.2. *Effect of Welding Speed*

The thermal history for different locations in the VP-GTAW process plays a significant role in determining the microstructure and mechanical properties of welded joints. The maximum fluid temperature as function of welding time can be extracted using the calculated temperature fields. Figure 10 shows the variations of maximum fluid temperature with welding speed and time. Keeping

the pulse frequency (3 Hz) constant, the welding heat source moved at different speeds u in the x-axis direction. It was found that the synchronous observation from welding time and maximum fluid temperature was very effective in confirming the torch position, and the upper and lower limits of maximum fluid temperature provided us with information about the transient weld pool dynamics.

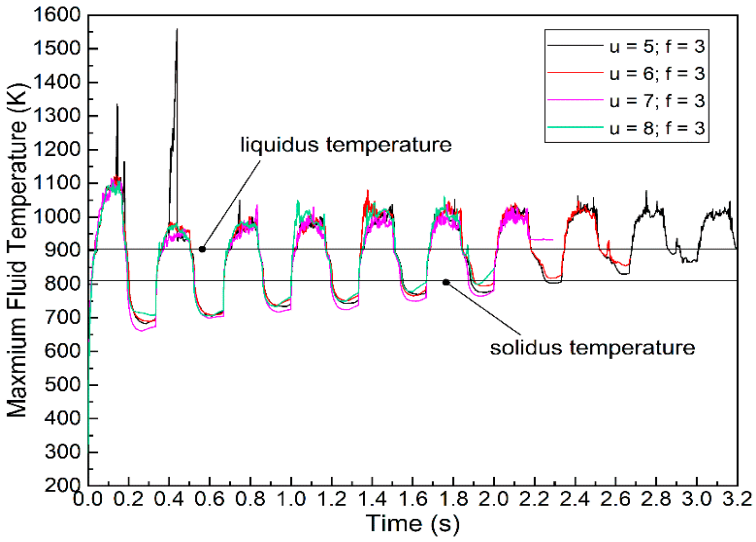


Figure 10. Variations of maximum fluid temperature with welding speed and time.

According to the calculated maximum fluid temperature values with time, the current type was DCEN phase at the beginning of welding, there was no preheating and the heat input became very concentrated, the large arc heat input produces rapid heating and melting, and then the weld pool was created in a very short time. Thus, the peak temperature reached in the weld pool was superimposed. As the welding current turned to its DCEP phase, the maximum solidification rate was obtained, then the peak temperature dropped below the solidus temperature until the weld pool was completely solidified.

However, in the middle stage of welding, there was periodic preheating, the workpiece had obtained certain thermal energy via heat conduction, and the weld pool became quasi-steady state. This was also due to the fact that the local higher temperature range was maintained accordingly for the accumulated heat and the continuous heat input was adequate to fuse more materials at high speed.

When the heat source moved to x = 24 mm, max temperature values with welding time can be seen in Figure 10. This means that the heat penetration was a little deeper and the maximum fluid temperature of the workpiece was gradually close to its liquidus temperature. The reason is that heat continued to build up during VP-GTA welding. Generally speaking, the weld pool temperature exhibited nonlinear periodic fluctuations.

In Figure 11 and Figure 13, some important characteristics of the weld beads, such as surface depression depth, width, and the pitch of humps, were quantitatively analyzed. The average values and amplitudes of these three variables were calculated and measured for different welding speeds and pulse frequencies. The maximum depth of the surface depression was almost calculated and measured on the basis of the surface of a solidified weld bead.

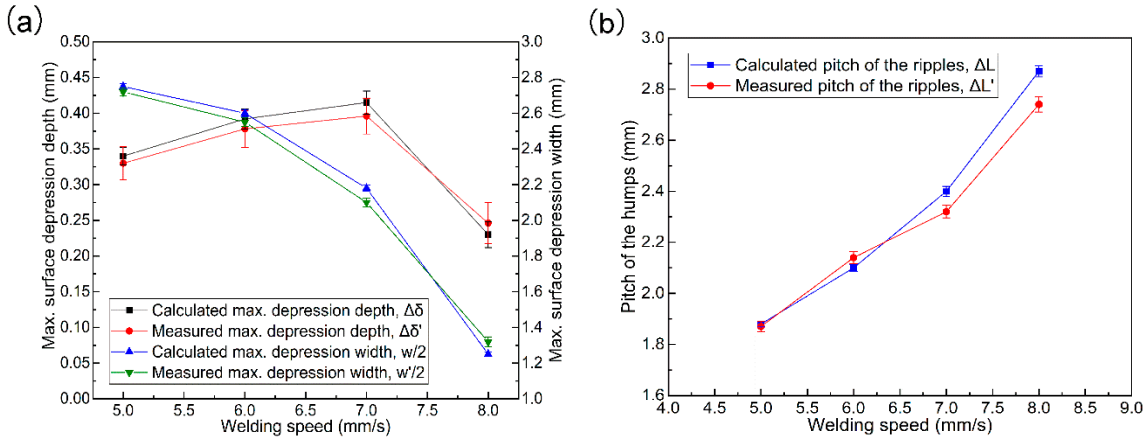


Figure 11. Calculated profiles of the weld pool depression with different welding speed: (**a**) weld pool depression, and (**b**) pitch of the humps.

Under the pulsed current condition, the surface depression was produced mainly via arc pressure and fluid flow patterns at peak duration. As illustrated in Figure 11, it was found that the surface depression increased for the higher welding speed of 7 mm/s. However, with the welding speed reaching to 8 mm/s, the effect of the welding speed on surface depression decreased. The reason is explained using the maximum fluid temperature in Figure 10. Slow welding speeds result in a hotter arc, increased penetration, and a wider weld bead. However, the Marangoni effect and hydrostatic pressure helped to fill the depressed pool center induced by arc pressure, which reduced the surface depression and its fluctuation. As the welding speed increased to 7 mm/s, the lower limit of maximum fluid temperature reached the lowest. During the VP-GTA welding process, that is to say, until 7 mm/s, the weld pool showed the lowest limit of maximum fluid temperature caused by a complex interaction between heat input, heat loss by conduction, and massive pool dynamics. It can also be seen from the figure that as the welding speed increased, the error values of the weld bead shape, both calculated and measured, had an increasing trend because of the complex interactions between thermal, mechanical, and metallurgical properties, and the fluid flow of the weld pool.

3.3. Effect of Pulse Frequency

The effect of pulse frequency on the maximum fluid temperature and surface depression are illustrated in Figures 12 and 13, respectively, where the DCEN and DCEP current of 240 and 120 A, respectively, and a corresponding welding speed of 8 mm/s was used for calculation.

When the pulse frequency was 1 Hz and DCEN duration was 500 ms, the weld pool size became larger after 0.13 s, and there was a more obvious time delay in the maximum fluid temperature because it took time to deliver heat via Marangoni convection in the larger weld pool.

Figure 13 shows the variation of the weld bead shape with pulse frequency. It can be seen that the weld bead geometry characteristics underwent a nonlinear decrease on the whole as pulse frequency increased.

From Figure 13a, it can be seen that as the pulse frequency and DCEN duration increased to 10 Hz and 50 ms, respectively, and the surface depression became smaller than that of others and the pitch of humps was almost equal to zero. This implies that the DCEN duration was an important factor in determining the surface depression, and a sufficiently long DCEN duration was needed to provide enough momentum within the weld pool. The errors caused by the increasing pulse frequency can be observed, and the largest errors occurred when using a single-pulse frequency, which was mainly attributed to the local thermal non-equilibrium effects at a lower pulse frequency. At a higher frequency, a weld bead with a stacked dimes appearance was easily created.

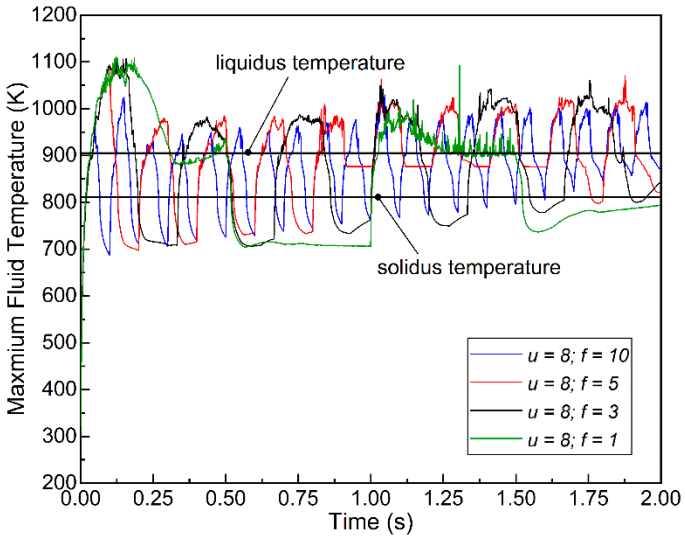


Figure 12. Variation of maximum fluid temperature with pulse frequency.

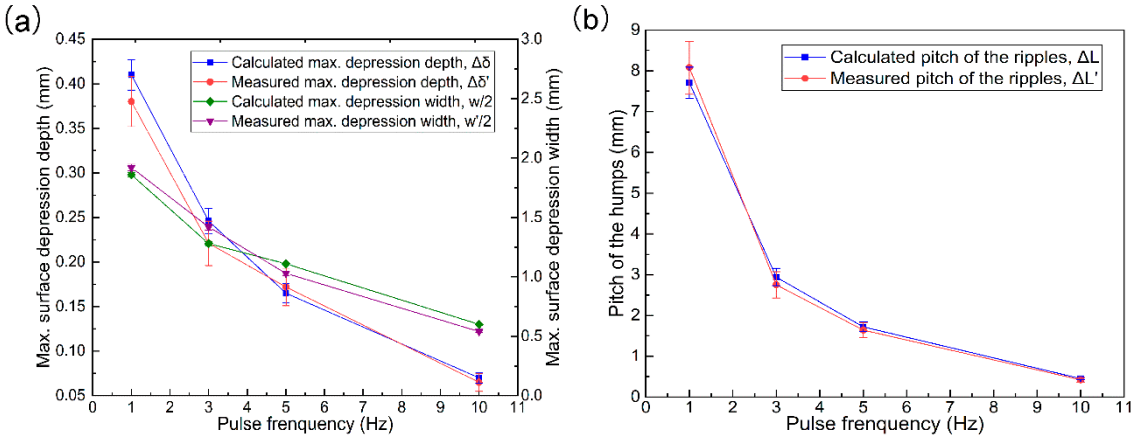


Figure 13. Calculated profiles of the weld pool depression with different pulse frequency: (**a**) weld pool depression, and (**b**) pitch of the humps.

4. Conclusions

For a VP-GTA welding process of Al alloy, a 3D numerical analysis model was developed by considering the weld pool depression, welding speed, pulse frequency, and their interrelations, which could describe the thermal and flow behaviors of the liquid metal. The validity of the numerical model was examined by comparing the weld bead geometries and experimental results. The conclusions drawn from this study are as below.

(1) Hump formation during high-speed VP-GTAW can be mainly attributed to the combined action of the fluctuation of the weld pool surface using an alternating transport current, the periodical variation of the cooling rates, and solidification growth rates in DCEN and DECP phase.

(2) Variation of maximum fluid temperature inside the workpiece during the VP-GTAW can provide valuable information for the prediction of transient diminution of weld pool and heat transfer characteristics in the welding process.

(3) An increasing pulse frequency of the welding current showed a decreasing potential trend for the surface depression and pitch of the humps. As the welding speed increased, DCEN duration decreased, thus the pitch of humps increased; however, the surface depression of the weld pool did not always increase monotonically.

The obtained results provide some insights and information (such as the correlations between welding process parameters and weld pool 3D thermal-flow behaviors and weld bead shape, and the

relationship between the maximum fluid temperature inside workpiece and transient diminution of weld pool) not available from experiments for optimizing the VP-GTAW process to achieve quality welds or weld profiles.

Author Contributions: J.D. conceived and designed the experiments, and composed the manuscript; G.Z. aided in the description of the thermo-physical properties of materials and implementation into CFD; Z.W. supervised throughout the experiments, and reviewed and edited the manuscript.

Funding: The research was financially supported by the State Key Development Program Research of China (2017YFB1103201), National Natural Science Foundation of China (Grant No. 51775420), and Zhejiang basic public welfare research plan (LGG18E050015).

Conflicts of Interest: The authors declare no conflict of interest.

Nomenclature

A_x, A_y, A_z	fractional area opening to the flow
a, b, c	heat source parameters (mm)
C_p	specific heat capacity (J kg^{-1} K^{-1})
d	diameter of the channel of fused-coating head (mm)
D	diameter of the end-face of fused-coating head (mm)
F	volume of fluid function
I	arc current (A)
k	thermal conductivity of alloy (W m^{-1} K^{-1})
L	thickness of workpiece (mm)
h	gap between the fused-coating head and workpiece (mm)
h_A	heat transfer coefficient between the liquid metal and workpiece
h_{sl}	latent heat of fusion (J kg^{-1})
P_{arc}	arc pressure (N/m^2)
q	volumetric heat density of weld pool (w/m^2)
R_c	radius of the surface curvature (mm)
r_{Shear}	arc drag force distribution parameter (mm)
T	temperature (K)
T_l	liquidus temperature (K)
T_s	solidus temperature (K)
T_{ev}	vaporization temperature (K)
T_∞	ambient temperature (K)
u	velocity in x-direction (mm/s)
U	workpiece moving speed (mm/s)
v	velocity in y-direction (mm/s)
V	volume flow rate of liquid metal (mm^3/s)
w	velocity in z-direction (mm/s)
x, y, z	
Greek symbols	
ρ	density (kg/m^3)
γ	surface tension coefficient (N/m)
μ	dynamic viscosity of liquid metal (N·s/m^2)
μ_0	magnetic permeability (H/m)
η	arc thermal efficiency
σ_r	arc pressure distribution parameter
ε	radiation emissivity
Subscripts	
en	DCEN phase
ep	DCEP phase
l	liquid phase
s	solid phase

References

1. Ostermann, F. *Anwendungstechnologie Aluminium*; Springer: Berlin/Heidelberg, Germany, 2014.
2. Wang, L.L.; Wei, J.H.; Wang, Z.M. Numerical and experimental investigations of variable polarity gas tungsten arc welding. *Int. J. Adv. Manuf. Technol.* **2018**, *95*, 2421–2428. [CrossRef]
3. Juang, S.C.; Tarng, Y.S. Process parameter selection for optimizing the weld pool geometry in the tungsten inert gas welding of stainless steel. *J. Mater. Process. Technol.* **2002**, *122*, 33–37. [CrossRef]
4. Kumar, A.; Sundarrajan, S. Selection of Welding Process Parameters for the Optimum Butt-Joint Strength of an Aluminum Alloy. *Mater. Manuf. Process.* **2006**, *21*, 779–782. [CrossRef]
5. Devakumaran, K.; Ghosh, P.K. Thermal Characteristics of Weld and HAZ during Pulse Current Gas Metal Arc Weld Bead Deposition on HSLA Steel Plate. *Mater. Manuf. Process.* **2010**, *25*, 616–630. [CrossRef]
6. Trautmann, M.; Hertel, M.; Füssel, U. Numerical simulation of TIG weld pool dynamics using smoothed particle hydrodynamics. *Int. J. Heat Mass Transf.* **2017**, *115*, 842–853. [CrossRef]
7. Pan, J.; Hu, S.; Yang, L.; Wang, D. Investigation of molten pool behavior and weld bead formation in VP-GTAW by numerical modelling. *Mater. Des.* **2016**, *111*, 600–607. [CrossRef]
8. Chen, W.; Chin, B. Monitoring joint penetration using infrared sensing techniques. *Weld. J.* **1990**, *69*, 181–185.
9. Vasudevan, M.; Chandrasekhar, N.; Maduraimuthu, V.; Bhaduri, A.K.; Raj, B. Real-Time Monitoring of Weld Pool during GTAW using Infra-Red Thermography and analysis of Infra-Red thermal images. *Weld. World* **2011**, *55*, 83–89. [CrossRef]
10. Liang, G.; Yuan, S. Study on the temperature measurement of AZ31B magnesium alloy in gas tungsten arc welding. *Mater. Lett.* **2008**, *62*, 2282–2284. [CrossRef]
11. Dutta, P.; Joshi, Y.; Janaswamy, R. Thermal modeling of gas tungsten arc welding process with nonaxisymmetric boundary conditions. *Numer. Heat Tranf. A Appl.* **1995**, *27*, 499–518. [CrossRef]
12. Farzadi, A.; Serajzadeh, S.; Kokabi, A.H. Investigation of weld pool in aluminum alloys: Geometry and solidification microstructure. *Int. J. Therm. Sci.* **2010**, *49*, 809–819. [CrossRef]
13. Farzadi, A.; Serajzadeh, S.; Kokabi, A.H. Prediction of solidification behaviour of weld pool through modelling of heat transfer and fluid flow during gas tungsten arc welding of commercial pure aluminium. *Mater. Sci. Technol.* **2008**, *24*, 1427–1432. [CrossRef]
14. Faraji, A.H.; Goodarzi, M.; Seyedein, S.H.; Zamani, M.H. Experimental study and numerical modeling of arc and weld pool in stationary GTA welding of pure aluminum. *Int. J. Adv. Manuf. Technol.* **2014**, *71*, 2059–2071. [CrossRef]
15. Pan, J.; Hu, S.; Yang, L.; Li, H. Simulation and analysis of heat transfer and fluid flow characteristics of variable polarity GTAW process based on a tungsten–arc-specimen coupled model. *Int. J. Heat Mass Transf.* **2016**, *96*, 346–352. [CrossRef]
16. Meng, X.; Qin, G.; Zou, Z. Investigation of humping defect in high speed gas tungsten arc welding by numerical modelling. *Mater. Des.* **2016**, *94*, 69–78. [CrossRef]
17. Campbell, S.W.; Galloway, A.M.; McPherson, N.A. Techno-economic evaluation of reducing shielding gas consumption in GMAW whilst maintaining weld quality. *Int. J. Adv. Manuf. Technol.* **2012**, *63*, 975–985. [CrossRef]
18. Ley, F.H.; Campbell, S.W.; Galloway, A.M.; McPherson, N.A. Effect of shielding gas parameters on weld metal thermal properties in gas metal arc welding. *Int. J. Adv. Manuf. Technol.* **2015**, *80*, 1213–1221. [CrossRef]
19. Hirt, C.W.; Nichols, B.D. Volume of fluid (VOF) method for the dynamics of free boundaries. *J. Comput. Phys.* **1981**, *39*, 201–225. [CrossRef]
20. Brackbill, J.U.; Kothe, D.B.; Zemach, C. A continuum method for modeling surface tension. *J. Comput. Phys.* **1992**, *100*, 335–354. [CrossRef]
21. Bibby, M.J.; Goldak, J.A.; Shing, G.Y. A Model for Predicting the Fusion and Heat-Affected Zone Sizes of Deep Penetration Welds. *Can. Metall. Q.* **1985**, *24*, 101–105. [CrossRef]
22. Desai, R.S.; Bag, S. Influence of displacement constraints in thermomechanical analysis of laser micro-spot welding process. *J. Manuf. Process.* **2014**, *16*, 264–275. [CrossRef]
23. Cho, D.W.; Lee, S.H.; Na, S.J. Characterization of welding arc and weld pool formation in vacuum gas hollow tungsten arc welding. *J. Mater. Process. Technol.* **2013**, *213*, 143–152. [CrossRef]
24. Sreedhar, U. Static GTAW: Experimental and Numerical Investigations and Heat Flux Parameter Estimation. Ph.D. Thesis, Universit´e Montpellier-II, Montpellier, France, 2014.

25. Cho, D.W.; Na, S.J.; Cho, M.H.; Lee, J.S. Simulations of weld pool dynamics in V-groove GTA and GMA welding. *Weld. World* **2013**, *57*, 223–233. [CrossRef]
26. Kou, S.; Sun, D.K. Fluid flow and weld penetration in stationary arc welds. *Metall. Mater. Trans. A* **1985**, *16*, 203–213. [CrossRef]
27. Christensen, N.; Davies, V.; Gjermundsen, K. The Distribution of Temperature in Arc Welding. *Br. Weld. J.* **1965**, *12*, 54–75.
28. Azar, A.S.; Ås, S.K.; Akselsen, O.M. Determination of welding heat source parameters from actual bead shape. *Comput. Mater. Sci.* **2012**, *54*, 176–182. [CrossRef]



© 2019 by the authors. Licensee MDPI, Basel, Switzerland. This article is an open access article distributed under the terms and conditions of the Creative Commons Attribution (CC BY) license (http://creativecommons.org/licenses/by/4.0/).